Article

Determination of Evaporative Fluxes Using a Bench-Scale Atmosphere Simulator

Jared Suchan [ID] and Shahid Azam *[ID]

Environmental Systems Engineering, Faculty of Engineering and Applied Science, University of Regina, 3737 Wascana Parkway, Regina, SK S4S 0A2, Canada; suchan1j@uregina.ca
* Correspondence: shahid.azam@uregina.ca

Abstract: An accurate determination of evaporative fluxes is critical for efficient water management in semi-arid climates such as in the Canadian Prairies. The main achievements of this research are the design and operation of a bench-scale atmosphere simulator, performance evaluation using selected weather scenarios pertaining to regional atmospheric conditions, validation using established empirical correlations, and estimation of evaporation rates and the amount for a typical local water body. Results indicate that the measured data achieved the target values for the various parameters and the data were found to be stable during the 3-h test duration. The vapour flux was found to have large variation during summer (0.120 g·s^{-1}·m^{-2} during the day and 0.047 g·s^{-1}·m^{-2} at night), low variation during spring (0.116 g·s^{-1}·m^{-2} during the day and 0.062 g·s^{-1}·m^{-2} at night), and negligible change during fall (0.100 g·s^{-1}·m^{-2} during the day and 0.076 g·s^{-1}·m^{-2} at night). The measured vapour flux was generally within one standard deviation of the equality line when compared with that predicted by both the mass-transfer equations and the combination equations. The average evaporation ranged from 4 mm·d^{-1} to 8 mm·d^{-1} during the day and decreased to 1 mm·d^{-1} to 3 mm·d^{-1} at night. The 24-h evaporation was found to be 8 ± 1 mm·d^{-1} from late April through late October. Likewise, the cumulative annual evaporation was found to be 1781 mm, of which 82% occurs during the day and 18% at night.

Keywords: bench scale; atmosphere simulator; evaporative fluxes; mass; energy; momentum

1. Introduction

Potential evaporation from open water bodies is a complex phenomenon because of the interactions between meteorological and physiological factors [1]. The net upward movement of vapour from an exposed water surface to the atmosphere depends on the interaction between atmospheric and surface parameters. The constitutive relationships are based on the laws of conservation for momentum, mass, and energy [2]. Several methods to determine evaporative fluxes from water surfaces are available in the literature [3–5]. The resulting empirical relationships for predicting potential evaporation require accurate field and/or laboratory measurements [6]. Field data is affected by spatial and temporal variations in atmospheric parameters and physiographic features and, as such, the resulting correlations are site-specific and assume constant climatic conditions [7]. For example, the variation in pan evaporation and estimated evaporation is reported to be governed by solar irradiation in an open lake in Australia [8]. Conversely, laboratory determination can create a simplified environment by isolating selected influencing parameters provided these are adequately replicated [9]. Most climate chambers only partially capture the various atmospheric components because of the difficulty arising from the interactions. Therefore, there is a need to understand the phenomenon of evaporation from a fundamental perspective.

The semi-arid Canadian Prairies have the highest water demand-to-availability ratio in Canada [10]. Low and spatiotemporally variable precipitation [11], a reliance on seasonally variable glacial runoff [12], interprovincial water use agreements [13], and competing

municipal and industrial requirements [14] pose an acute risk to water security in the area. More than 70 storage facilities have been constructed to manage the regional water supply [15]. The large surface areas of these shallow water bodies facilitate evaporation [16]. In particular, the surface area of Lake Diefenbaker varies from 102–430 km^2, such that a 10 mm elevation drop results in a water loss of 1–4.3×10^6 m^3 [17]. The annual evaporation in this man-made reservoir is estimated to be up to 1000 mm [18] thereby accounting for more than all other withdrawals combined [19]. Furthermore, the upcoming irrigation project proposes to extract 850×10^6 m^3 of water from the lake which is almost twice the estimated annual evaporation [20]. To ensure uninterrupted availability of water for all purposes, there is an exigent need to understand evaporation from Lake Diefenbaker.

The main objective of this paper is to determine evaporative fluxes using a de novo bench-scale atmosphere simulator (BAS). First, the design and operation of the climate chamber and the supporting modules are presented. Second, the performance of BAS was evaluated using selected weather scenarios pertaining to regional atmospheric conditions. Third, the measured and analysed data were validated using established empirical correlations. Fourth, potential evaporation rates and the amount for a typical local water body were estimated.

2. Design and Operation of the BAS

The BAS was designed to capture the main atmospheric parameters affecting evaporation particularly those operating in the region: (i) solar irradiance because the surface receives 220 W/m^2 for up to 16 h/d in the spring, 240 W/m^2 in the summer for 17 h/d, and 105 W/m^2 for 13 h/d in fall in Saskatchewan, and the area receives the highest annual radiant energy (154 W/m^2 in Regina) in Canada [21]; (ii) wind effects because of turbulent transport due to a flat area devoid of physical buffers such that wind speeds generally vary between 16 and 21 km/h (measured at 2 m above the surface) throughout the year [11], and; (iii) air temperature and humidity because of the warm and dry climate (*Dfb* according to Köppen–Geiger classification) and the significance of fetch effects [22].

Figure 1 gives a schematic of the BAS. The system layout comprises the climate chamber (Figure 2) and supporting modules (Figure 3) that were configured to govern the atmospheric parameters of air velocity, humidity, temperature, and solar irradiance. The BAS worked on the modular operation of the individual components. To create steady-state meteorological conditions during testing, the various modules were adjusted and the desired atmospheric parameters were achieved within a conditioning period of 0.5 to 1.5 h.
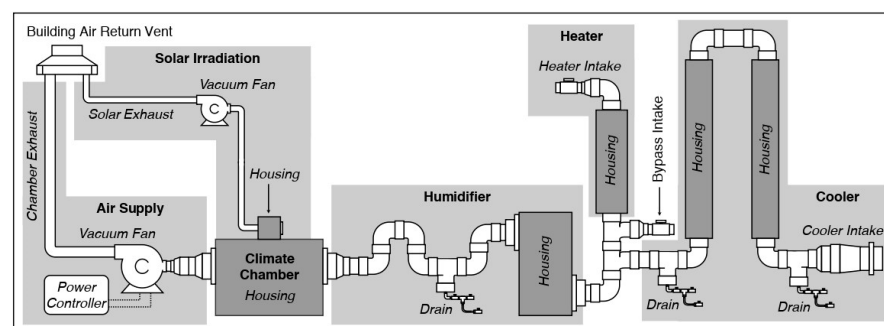

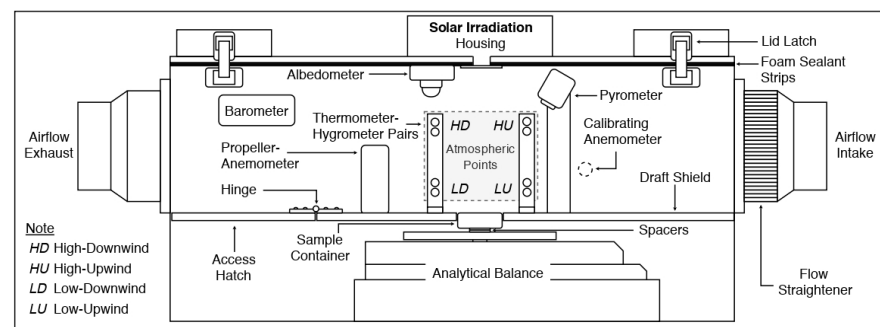**Figure 1.** System layout of bench-scale atmosphere simulator.
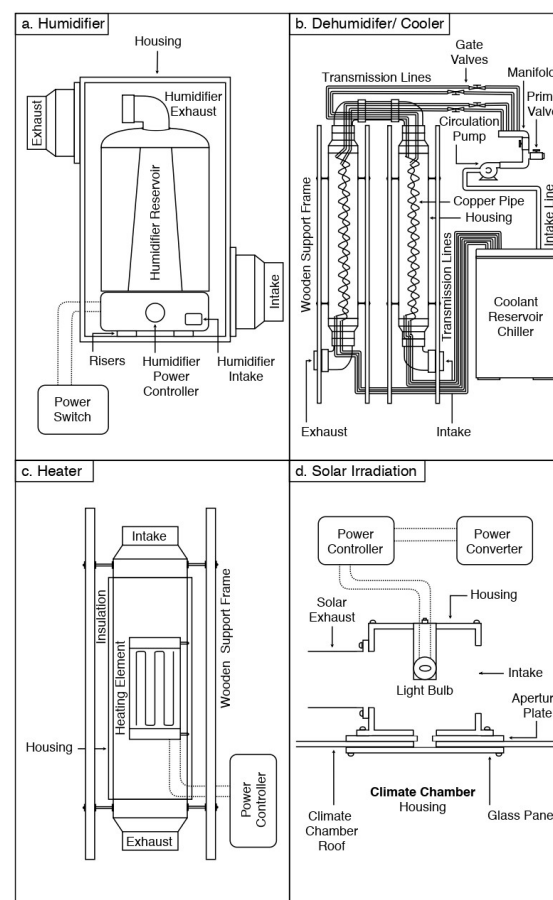
Figure 2. Schematic of the climate chamber.

Figure 3. Schematic of the supporting modules: (**a**) humidifier, (**b**) dehumidifier/cooler, (**c**) heater, and (**d**) solar irradiation.

The *climate chamber* was designed to measure a number of parameters in the atmospheric and surface layers. The sensor dimensions, technical details, measuring principles, accuracy and precision are not given in this paper. The various sensors were arranged around the sample surface to preclude interferences and data were usually recorded at 10-s intervals. The air velocity was measured 65 mm behind the sample centre and 30 mm above the surface by a propeller-type anemometer (60 mm diameter). Air turbulence above the surface was reduced and assumed negligible by the incorporation of a flow straightener [23] and draft shield [24]. Air pressure in the chamber was recorded by a wall-mounted barometer. Air temperature and relative humidity, recorded by thermometers and hygrometers, were measured at four points: *low* (25 mm above surface); *high* (75 mm above surface); *upwind* (50 mm before sample centre); and *downwind* (50 mm after sample centre). Values of absolute humidity are also reported to represent a measure of water in air

irrespective of temperature. Sample mass was recorded by an analytical balance. Surface temperature was measured approximately 95 mm above the surface using a pyrometer. Incoming and outgoing shortwave radiant energy (285 nm to 3 μm), recorded before and after each experiment by a pyranometer and albedometer, were measured at surface level and about 125 mm above. The corresponding longwave radiant energy (8 to 14 μm) were estimated [25]. Atmospheric sensor data were displayed on digital readouts in real-time, thereby allowing parameter re-adjustments when required.

The *air supply* (Figure 1) design was based on an open-air and non-return wind tunnel [26] with air sucked by a fan at a controlled flow rate [27]. The simple open-air and non-return design completely isolated the BAS from interfering with ambient humidity and temperature.

Likewise, the fan-driven suction precluded possible pumping effects [28]. An ultrasonic *humidifier* (Figure 3a) was used to increase vapour content in the air [29]. In contrast, the *cooler/dehumidifier* (Figure 3b) used a glycol chiller to decrease vapour content and remove thermal energy from the air [9]. Finally, the *heater* (Figure 3c) used an electric element to add thermal energy to the air [30].

The *solar irradiation* module (Figure 3d) used a 275 W quartz-tungsten-halogen (QTH) bulb (~225 mm above the surface) to mimic the irradiant shortwave energy and spectral pattern of the sun [31]. The externally mounted module ensured clear separation of shortwave and longwave bands thereby closely replicating actual conditions. The thermal heat generated by the QTH bulb was removed by a vacuum-fan suction system [32]. The power controller was adjusted to ensure that the sample received the desired shortwave irradiance, as measured by the pyranometer.

3. Research Methodology

Vapour flux tests were conducted based on atmospheric parameters in the study area. For each test, the sample container was cleaned with distilled water, allowed to air dry, and placed on the analytical scale balance. The balance was tared with the empty container and approximately 15 mL of room temperature distilled water was added through a syringe. Data logging sensors were turned on and the climate chamber lid was closed, and modules relevant to the active weather scenario were engaged. After the desired atmospheric conditions in the chamber were attained, the lid was re-opened and ~15 mg of water added. The evaporation tests were conducted for 3.0 h, similar to [33], to obtain sufficient data while maintaining constant meteorological conditions in the BAS. This generated 1100 measurements at 10-s intervals. The average vapour flux over the course of each experiment was determined using the change in sample mass over time, and the surface area of the sample.

Table 1 provides the average atmospheric parameters for the selected weather scenarios (spring, summer, and fall) showing both daytime and nighttime values. Winter was not included because freezing conditions are prevalent during this season. The atmospheric parameters (hourly land-based measurements) were obtained from the Canadian Weather Energy and Engineering Datasets (CWEEDS). Based on data from 1998 to 2014, the variations of atmospheric parameters were plotted in the form of mean values and standard deviation over the year. The selected value of each parameter was horizontally extended and a distinct change in standard deviation was identified as the cut-off date for a given season.

Figure 4 presents typical annual daytime conditions in the study area with the summer weather scenario highlighted. The atmospheric parameters represent the weighted average values between the stations surrounding Lake Diefenbaker: Regina (172 km), Swift Current (117 km), Wynyard (196 km), and Kindersley (170 km). The measured values of atmospheric parameters at a station were divided by their respective distances from Lake Diefenbaker and averaged using the sum of the inverse distances following the method [34]. The presented data were used to simulate evaporative conditions at the water surface. The air velocity (Figure 4a) data were downscaled using the method described by [35].

Likewise, the air humidity (Figure 4b), presented as vapour density, was calculated from partial vapour pressure using dewpoint temperature and air temperature, as given in Figure 4c [36]. Solar irradiance (Figure 4d) represents the sum of direct and diffuse radiant energy received at the ground surface. Finally, the water surface temperature (Figure 4e) of a 1.0 km² section on Lake Diefenbaker was obtained using the Oak Ridge National Laboratory (ORNL) MODIS Land Product Subset Tool—MYD21A2 that contains 17-years (2002 to 2019) of 8-day water-based measurements [37].

Table 1. Selected atmospheric parameters in the study area.

Weather. Scenario	Date Range (Day Number)	Duration (Hours)	Air Velocity (m·s^{-1}) [a]	Air Humidity (g·m^{-3}) [b]	Air Temperature (°C)	Solar Irradiance (W·m^{-2}) [c]	Surface Temperature (°C)
Day	84–334	3706					
Spring	94–149	883	1.7	5.0	10.0	325	11.8
Summer	150–254	1755	1.3	9.0	19.0	325	21.8
Fall	261–304	541	1.6	5.0	9.0	210	12.9
Night	110–317	1827					
Spring	122–148	206	1.3	5.0	9.0	0	6.1
Summer	149–253	761	1.3	8.5	13.0	0	16.5
Fall	254–279	277	1.5	5.5	9.0	0	15.9

[a] Downscaled from CWEEDS 10 m anemometer height to BAS 0.03 m height using the Logarithmic Law. [b] Absolute humidity (vapour density) calculated using CWEEDS dewpoint temperature and dry bulb temperature. [c] Global solar horizontal irradiance at the surface, shortwave spectrum (285 nm to 3 μm).
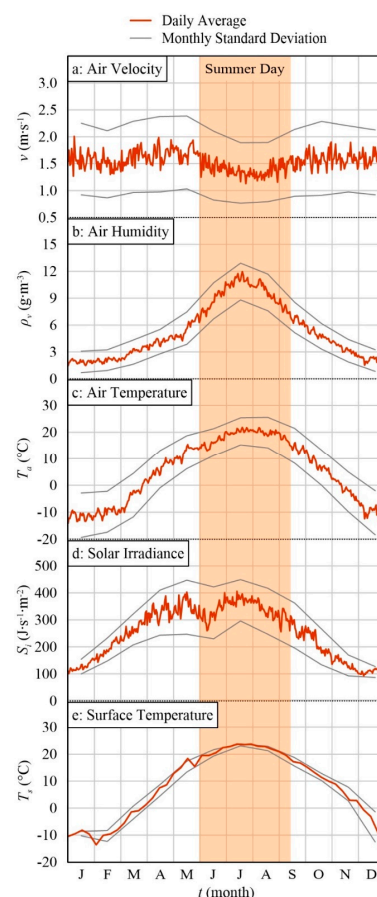

Figure 4. Typical day time atmospheric and water surface conditions in the study area: (**a**) air velocity, (**b**) air humidity, (**c**) air temperature, (**d**) solar irradiance, and (**e**) surface temperature.

4. Results and Discussion

Table 2 provides a summary of the average atmospheric and water surface parameter measurements in the BAS for the investigated weather scenarios. The standard error

over the test duration for each of the parameters was found to be negligible, thereby demonstrating that the BAS is able to maintain steady-state atmospheric conditions. The target air velocity (Table 1) was achieved in the BAS. Depending on the weather scenario, the air pressure measured from about 93 kPa to 96 kPa. The variation in relative humidity and air temperature among the four sensors is attributed to their fetch location with respect to the sample. Generally, the *upwind* and *high* sensors measured low relative humidity and high air temperature compared to their *downwind* and *low* counterparts. This is attributed to wind direction (which laterally moves the water vapour released from the sample surface [38]) and elevation (which retards the vertical movement of water vapour released from the sample [39]). Based on the average of the lower sensors, the target air temperature (Table 1) was achieved in the BAS. With the target incoming shortwave flux (Table 1) achieved in the BAS, the outgoing shortwave flux was found to be lower than the suggested albedo coefficient for open water bodies [5]. This is primarily attributed to the stationary and perpendicular flux source as opposed to the moving and angular direction of the sun [40]. The rate of mass change due to evaporation over 3-h was obtained using ten-degree polynomial regression curves that best-fitted the measured data. The resulting values were found to range between 7×10^{-3} g·s⁻¹ to 18×10^{-3} g·s⁻¹. Finally, the surface temperature followed the expected seasonal and day-night trends that may be partially attributed to the specific heat capacity of water. Given the short test duration and small sample size, the measured data do not capture the long-term heat storage effects of deep water bodies [41].

Table 2. Summary of average experimental atmospheric and water surface parameter measurements.

Parameter	Unit	Symbol	Weather Scenario					
			Day			Night		
			Spring	Summer	Fall	Spring	Summer	Fall
Atmosphere								
Momentum								
Velocity	m·s⁻¹	v	1.7 ± 0.0	1.3 ± 0.0	1.6 ± 0.0	1.3 ± 0.0	1.3 ± 0.0	1.5 ± 0.0
Mass								
Air Pressure	Pa	e_a	93,612 ± 3	96,279 ± 5	93,182 ± 2	96,302 ± 3	94,065 ± 4	92,853 ± 2
Relative Humidity								
Upwind, High	%	h_{UH}	34.0 ± 0.0	46.6 ± 0.1	37.9 ± 0.0	40.9 ± 0.1	59.1 ± 0.1	43.0 ± 0.0
Downwind, High	%	h_{DH}	41.9 ± 0.0	47.4 ± 0.1	44.3 ± 0.0	44.1 ± 0.1	63.4 ± 0.1	46.4 ± 0.0
Upwind, Low	%	h_{UL}	48.0 ± 0.1	51.2 ± 0.1	49.7 ± 0.1	53.6 ± 0.1	70.5 ± 0.1	52.9 ± 0.0
Downwind, Low	%	h_{DL}	59.2 ± 0.1	55.0 ± 0.1	59.0 ± 0.1	62.9 ± 0.2	78.4 ± 0.1	60.0 ± 0.0
Energy								
Temperature								
Upwind, High	°C	T_{aUH}	16.3 ± 0.0	21.4 ± 0.0	15.2 ± 0.0	12.9 ± 0.0	15.5 ± 0.0	14.8 ± 0.0
Downwind, High	°C	T_{aDH}	13.4 ± 0.0	20.8 ± 0.0	12.6 ± 0.0	11.9 ± 0.0	14.7 ± 0.0	13.6 ± 0.0
Upwind, Low	°C	T_{aUL}	11.3 ± 0.0	19.5 ± 0.0	10.4 ± 0.0	9.6 ± 0.0	13.6 ± 0.0	11.1 ± 0.0
Downwind, Low	°C	T_{aDL}	9.3 ± 0.0	18.9 ± 0.0	8.7 ± 0.0	8.3 ± 0.0	12.7 ± 0.0	10.1 ± 0.0
Shortwave Flux (↓)	W·m⁻²	S_i	325 ± 0	325 ± 0	210 ± 0	0 ± 0	0 ± 0	0 ± 0
Surface								
Mass								
Rate of Mass Change	g·s⁻¹	ΔM	17.5 × 10⁻³ ± 0	18.1 × 10⁻³ ± 0	15.1 × 10⁻³ ± 0	9.32 × 10⁻³ ± 0	7.08 × 10⁻³ ± 0	14.4 × 10⁻³ ± 0
Coefficient of Determination [a]		R^2	0.99	0.99	0.99	0.99	0.99	0.99
Energy								
Shortwave Flux (↑)	W·m⁻²	S_o	1 ± 0	1 ± 0	0 ± 0	0 ± 0	0 ± 0	0 ± 0
Temperature	°C	T_s	15 ± 0	18 ± 0	10 ± 0	7 ± 0	11 ± 0	9 ± 0

Note. The ± indicates the standard error (SE) of measurement within the 3-h test period ($n = 1100$) of the weather scenario [a] Applies to the fitted high-order polynomial curve used to determine rate of mass change (ΔM).

Figure 5 presents the typical atmospheric and water surface conditions measured over the test duration in the BAS for a summer day. The air velocity (Figure 5a) matched the target value of 1.3 m·s⁻¹ with minor fluctuations. The downward trend in air humidity (Figure 5b) from the target value of 9 g·m⁻³ is attributed to possible interference with the unregulated laboratory humidity. Such interferences were not observed with air temperature (Figure 5c), which was controlled in the laboratory. The target air temperature of 19 °C was achieved, as measured by the lower sensors. The variation in measured relative humidity and air temperature is due to the interrelationship of the two parameters [42]. The solar irradiance (Figure 5d) measurements before and after testing showed no deviation from the set calibration voltage and achieved the target value. Finally, the water surface temperature (Figure 5e) was noted to be stable during testing with the sporadic spikes attributable to the relatively lower precision (1 °C) of the pyrometer.

Table 3 gives a summary of the analysed data of average atmospheric and water surface parameters for the investigated weather scenarios. The corresponding transient data (not given in this paper) were found to be steady. From a momentum perspective, the aerodynamic resistance is a pertinent parameter affecting evaporation in the BAS. This parameter captures the atmospheric turbulent diffusion of mass and energy and is inversely related to wind velocity and cover height [5]. The values of aerodynamic resistance were found to range from 41 s·m^{-1} to 47 s·m^{-1} (typical for water surfaces) such that the lower values in spring and fall were associated with high wind velocity and the reverse was true for summer.
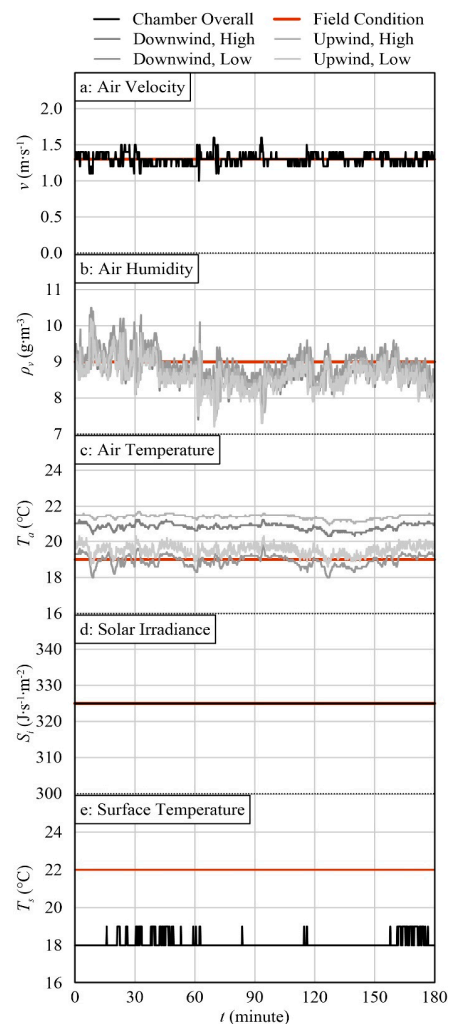

Figure 5. Typical atmospheric and water surface condition in the BAS for a summer day: (**a**) air velocity, (**b**) air humidity, (**c**) air temperature, (**d**) solar irradiance, and (**e**) surface temperature.

The target air humidity (Table 1) was achieved in the BAS as represented by vapour density. The vapour pressure deficit characterises the ease of evaporative mass transfer based on the residual water vapour capacity in the atmosphere that, in turn, depends on the temperature source and its measurement location [43]. The vapour pressure deficits were found to be generally high during the day as compared to those at night. In the BAS atmosphere, the data indicated large variation in vapour pressure deficit during summer (1047 Pa during the day and 389 Pa at night), low variation during spring (588 Pa during the day and 483 Pa at night), and negligible change fall (549 Pa during the day and 559 Pa at night). Likewise, the surface water data indicated large variations in vapour pressure deficit during spring (1037 Pa during the day and 353 Pa at night) and summer (898 Pa during the day and 190 Pa at night), and low variation during fall (559 Pa during the day

and 439 Pa at night). The separate determination of air and surface deficits allows for their subsequent use in the various empirical equations, as described later in this paper.

Assuming an infinitely thin surface with no heat storage, the available energy (Q) was calculated according to the following equation [44]:

$$Q = R - G = H + \lambda E \tag{1}$$

In the above equation, net radiant heat flux (R) was determined by measuring shortwave energy (Table 2) and estimating longwave energy (Table 3). Likewise, sensible heat flux (H) was determined using the Bowen Ratio and evaporative heat flux (λE). The ground heat flux (G) was determined by rearranging Equation (1) and solving using the measured and analysed variables. The available energy was found to be highest during spring (328 J·s^{-1}·m^{-2} during the day and 67 J·s^{-1}·m^{-2} at night), followed by summer (252 J·s^{-1}·m^{-2} during the day and 30 J·s^{-1}·m^{-2} at night), and then by fall (241 J·s^{-1}·m^{-2} during the day and 102 J·s^{-1}·m^{-2} at night).

The vapour flux was obtained from the measured rate of change in mass and the surface area. The data followed seasonal patterns similar to the atmospheric vapour pressure deficit, namely: a large variation during summer (0.120 g·s^{-1}·m^{-2} during the day and 0.047 g·s^{-1}·m^{-2} at night), a low variation during spring (0.116 g·s^{-1}·m^{-2} during the day and 0.062 g·s^{-1}·m^{-2} at night), and a negligible change during fall (0.100 g·s^{-1}·m^{-2} during the day and 0.076 g·s^{-1}·m^{-2} at night).

Figure 6 presents the effect of measured and analysed parameters on vapour flux. For measured parameters, the vapour flux showed opposite patterns for the night when compared to the day. This highlights the significance of capturing solar irradiance in the BAS, albeit more data is required to validate the observed patterns. Despite data scarcity, vapour flux generally increased with an increase in both vapour pressure deficit and energy, such that the night values were lower than the day values. The scatter in aerodynamic resistance is attributed to that in measured air velocity.
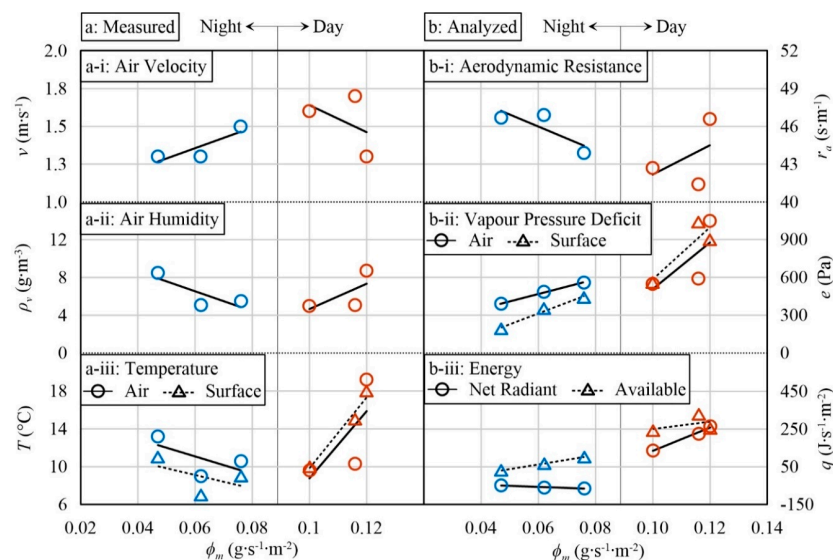

Figure 6. Effect of measured and analysed parameters on vapour flux (ϕ_m): (**a-i**) air velocity, (**a-ii**) air humidity, (**a-iii**) air and surface temperatures, (**b-i**) aerodynamic resistance, (**b-ii**) air and surface vapour pressure deficits, and (**b-iii**) net radiant and available energy.

Table 3. Summary of average atmospheric and water surface parameter analyses.

| Parameter | Unit | Symbol | Weather Scenario | | | | | |
| | | | Day | | | Night | | |
			Spring	Summer	Fall	Spring	Summer	Fall
Atmosphere								
Momentum								
Aerodynamic Resistance	$s \cdot m^{-1}$	r_a	41.4	46.6	42.7	46.9	46.7	43.9
Mass								
Vapour Density	$g \cdot m^{-3}$	ρ_v	5.1	8.8	5.0	5.1	8.5	5.5
Vapour Pressure								
Partial	Pa	e_v	668	1182	646	666	1125	721
Saturated	Pa	e_s	1256	2229	1196	1148	1514	1280
Deficit	Pa	e_d	588	1047	549	483	389	559
Energy								
Longwave Flux ($\downarrow$)	$J \cdot s^{-1} \cdot m^{-2}$	L_i	285	339	282	280	315	288
Surface								
Mass								
Vapour Pressure								
Saturated	Pa	e_f	1705	2080	1205	992	1315	1160
Deficit	Pa	e_u	1037	898	559	353	190	439
Energy								
Longwave Flux ($\uparrow$)	$J \cdot s^{-1} \cdot m^{-2}$	L_o	383	400	356	326	362	353
Net Radiant Heat Flux	$J \cdot s^{-1} \cdot m^{-2}$	R	226	264	136	−61	−48	−64
Evaporative Heat Flux	$J \cdot s^{-1} \cdot m^{-2}$	λE	287	294	247	153	115	187
Sensible Heat Flux	$J \cdot s^{-1} \cdot m^{-2}$	H	41	−43	−57	−94	−87	−86
Ground Heat Flux	$J \cdot s^{-1} \cdot m^{-2}$	G	−101	12	−55	−131	−79	−166
Available Energy	$J \cdot s^{-1} \cdot m^{-2}$	Q	328	252	241	67	30	102
Vapour Flux	$g \cdot s^{-1} \cdot m^{-2}$	ϕ	0.116	0.120	0.100	0.062	0.047	0.076

Figure 7 gives a comparison of the measured values with estimates based on empirical relationships and Table 4 gives the established empirical equations for potential evaporation relevant to the collected BAS data. The mass-transfer models used equations requiring variables of momentum and mass. These are based on Dalton's law of partial pressures and the eddy motion transfer of vapour from water surfaces into the atmosphere [45]. In contrast, the combination models included energy variables. As such, these models are designed to accommodate the effects of solar radiation and ground heat flux [6].

Table 4. Summary of empirical equations for estimation of vapour flux.

Reference and Type	*RMSE*	R^2	*SI*	Vapour Flux Equation ($g \cdot m^{-2} \cdot s^{-1}$)
[48], Mass-Transfer	0.028	0.90	0.33	$1 \times 10^{-6}(64.58 + 28.06v)e_d$
[49], Mass-Transfer	0.022	0.92	0.25	$1.06317 \times 10^{-7}\rho_w(1 + 0.1v)(e_d/1000)$
[46], Mass-Transfer	0.020	0.91	0.24	$3.3828 \times 10^{-8}\rho_w(1 + 0.24v)(e_d/1000)$
[47], Combination	0.011	0.99	0.12	$\frac{1}{\lambda}\left(\frac{\Delta Q + 1.01\rho_a e_u/r_a}{\Delta + \gamma}\right)$
[50], Combination	0.027	0.93	0.31	$\frac{1}{\lambda}\left[\frac{\Delta Q}{(0.85\Delta) + (0.63\gamma)}\right]$
[51], Combination	0.028	0.93	0.33	$\frac{1}{\lambda}\left[\frac{Q - (1.01\rho_a[-0.17T_a + 4.27][1 + 0.536v])}{251}\right]$

Note. Equations are adapted for appropriate units, as provided in Tables 2 and 3. *RMSE* is root mean square error, R^2 is correlation coefficient, and *SI* is scatter index.
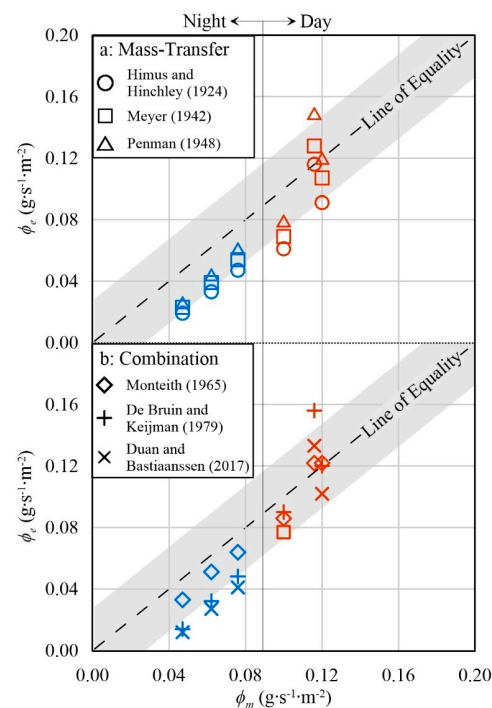
Figure 7. Comparison of estimated vapour flux (ϕ_e) and measured vapour flux (ϕ_m) based on: (**a**) mass-transfer equations and (**b**) combination equations.

The measured vapour flux was generally within one standard deviation of the equality line when compared with that predicted by both the mass-transfer equations (Figure 7a) and the combination equations (Figure 7b). The underestimated predictions are attributed to a downscaled air velocity in the BAS and/or the selected constants in the empirical equations. Among the former set, the equation by [46] was found to be closest to the measured data owing to a better prediction of the wind function. Likewise, the combination equation by [47] best matched the measured values due to the inclusion of atmospheric vapour pressure deficit. Finally, the vapour flux measured up to 0.12 g·s^{-1}·m^{-2} and this number does not pertain to any limitations of BAS.

Figure 8 gives predicted evaporation for the study area and Table 5 compares the results. The estimates based on BAS measurements (Figure 8a) are validated using representative empirical equations in Figure 8b (Meyer equation because it has been traditionally used in the investigated area) and in Figure 8c (Monteith equation because of its extensive use worldwide). The daily evaporation (E) for the various weather scenarios was determined using vapour flux (Table 3) and duration (Table 1) along with water density. During the day time, the BAS data predicted 1459 mm/year of evaporation that was 9% higher than that estimated by the mass-based Meyer equation but identical to the combination-based Monteith equation. During the night time, the BAS data predicted 322 mm/year of evaporation, which was over predicted by 39% and 27%, respectively. This might be attributed to less adequate chamber insulation for relatively cooler scenarios. Nonetheless, the average daily evaporation ranged from 4 mm·day^{-1} to 8 mm·day^{-1} during the day and decreased to 1 mm·day^{-1} to 3 mm·day^{-1} at night. The combined 24-h evaporation was found to be 8 ± 1 mm·day^{-1} from late April through late October. This is similar to the estimated data reported by [52] for Lake Diefenbaker. Furthermore, the cumulative annual evaporation was found to be 1781 mm, of which 82% occurs during the day and 18% during the night. Overall, the BAS over predicted the cumulative annual evaporation from the above-mentioned estimates by 15% and 4%, respectively.
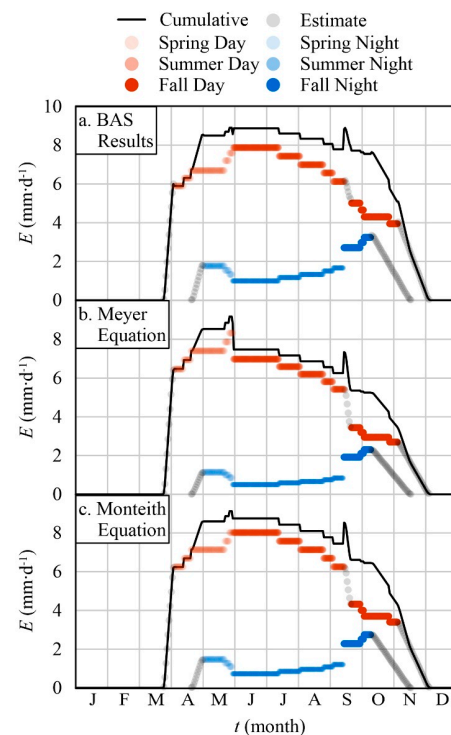
Figure 8. Predicted evaporation for the study area using: (**a**) BAS results; (**b**) Meyer equation; and (**c**) Monteith equation.

Table 5. Comparative summary of predicted evaporation for the study area.

Cumulative Evaporation	Amount (mm) and Percent Error from BAS		
	BAS	Meyer	Monteith
Annual	1781	1517 (−15%)	1711 (−4%)
Day	1459	1321 (−9%)	1457 (0%)
Night	322	196 (−39%)	254 (−27%)

The BAS effectively captured horizontal advection (fetch effects) through an adequate sensor placement. The analysed data must be understood in the context of land-surface transitions at shorelines, heat advection from inflowing water, and variable heat storage across the reservoir [53]. The seasonal values are partly affected by the long-term heat storage in the investigated water body [41]. In the absence of surface-atmosphere monitoring data, laboratory simulations can only be correlated with relevant empirical equations. Although the BAS cannot measure three-dimensional air velocity (eddy covariance) or be used for long-term studies, it can simulate various weather parameters that are required for the estimation of evaporation. This will help in informed decision making related to water storage and usage in the region, especially when coupled with field observations.

5. Summary and Conclusions

Knowledge of evaporation is critical for efficient water management in semi-arid climates such as in the Canadian Prairies. This research focused on determining evaporative fluxes using a de novo bench-scale atmosphere simulator that specifically captured the shortwave energy and spectral pattern of the sun. The system is capable of imposing atmospheric conditions on a sample of distilled water. While there are inherent limitations in laboratory investigations, this undertaking allowed a clear understanding of complicated interactions of mass and energy at water surfaces. This means that the findings correlate well with empirical relationships and, as such, are useful in water resources management. Based on regional atmospheric conditions, seasonal weather scenarios representing spring,

summer, and fall, were simulated under controlled air velocity, humidity, temperature, and solar irradiance. The main conclusions of this study are given below:

- All of the measured data achieved the target values for the various parameters and the data were found to be stable during the 3-h test duration. The slight downward trend in air humidity with respect to the target value is attributed to interferences with the unregulated laboratory humidity.

- The vapour flux was found to have large variation during summer (0.120 $g \cdot s^{-1} \cdot m^{-2}$ during the day and 0.047 $g \cdot s^{-1} \cdot m^{-2}$ at night), low variation during spring (0.116 $g \cdot s^{-1} \cdot m^{-2}$ during the day and 0.062 $g \cdot s^{-1} \cdot m^{-2}$ at night), and negligible change during fall (0.100 $g \cdot s^{-1} \cdot m^{-2}$ during the day and 0.076 $g \cdot s^{-1} \cdot m^{-2}$ at night).

- The measured vapour flux was generally within one standard deviation of the equality line when compared with that predicted by both the mass-transfer equations and the combination equations. The underestimated predictions are attributed to a down-scaled air velocity in the simulator and/or the selected constants in the empirical equations.

- The average evaporation ranged from 4 $mm \cdot d^{-1}$ to 8 $mm \cdot d^{-1}$ during the day and decreased to 1 $mm \cdot d^{-1}$ to 3 $mm \cdot d^{-1}$ at night. The 24-h evaporation was found to be 8 ± 1 $mm \cdot d^{-1}$ from late April through late October. Likewise, the cumulative annual evaporation was found to be 1781 mm, of which 82% occurs during the day and 18% at night.

References

1. Labedzki, L. *Evapotranspiration*; InTech: Rijeka, Croatia, 2011.
2. Bird, R.B.; Stewart, W.E.; Lightfoot, E.N.; Klingenberg, D.J. *Introductory Transport Phenomena*; Wiley: Hoboken, NJ, USA, 2015.
3. Shoko, C.; Dube, T.; Clark, D. Total evaporation estimation for accurate water accounting purposes: An appraisal of various available estimation methods. *Geocarto. Int.* **2017**, *32*, 1333–1351. [CrossRef]
4. Finch, J.W.; Hall, R.L. *Estimation of Open Water Evaporation: A Review of Methods*; Environment Agency: Bristol, UK, 2001.
5. Shuttleworth, W.J. Evaporation. In *Handbook of Hydrology*; Maidment, D.R., Ed.; McGraw-Hill Inc.: New York, NY, USA, 1993; pp. 4.1–4.53.
6. Finch, J.W.; Calver, A. *Methods for the Quantification of Evaporation from Lakes*; Centre for Ecology & Hydrology: Oxfordshire, UK, 2008.
7. Sartori, E. A critical review on equations employed for the calculation of the evaporation rate from free water surfaces. *Sol. Energy* **2000**, *68*, 77–89. [CrossRef]
8. Yihdego, Y.; Webb, J.A. Comparison of evaporation rate on open water bodies: Energy balance estimate versus measured pan. *J. Water Clim. Change* **2018**, *9*, 101–111. [CrossRef]
9. Trautz, A.C.; Illangasekare, T.H.; Howington, S. Experimental Testing Scale Considerations for the Investigation of Bare-Soil Evaporation Dynamics in the Presence of Sustained Above-Ground Airflow. *Water Resour. Res.* **2018**, *54*, 8963–8982. [CrossRef]
10. Faurès, J.M.; Hoogeveen, J.; Winpenny, J.; Steduto, P.; Burke, J. *Coping with Water Scarcity: An Action Framework for Agriculture and Food Security*; Food and Agriculture Organization of the United Nations: Rome, Italy, 2012.
11. Akhter, A.; Azam, S. Flood-Drought Hazard Assessment for a Flat Clayey Deposit in the Canadian Prairies. *J. Environ. Inform. Lett.* **2019**, *1*, 8–19. [CrossRef]
12. Fang, X.; Pomeroy, J.W. Drought impacts on Canadian prairie wetland snow hydrology. *Hydrol. Process.* **2008**, *22*, 2858–2873. [CrossRef]

13. Cutlac, I.-M.; Horbulyk, T. Optimal Water Allocation under Short-Run Water Scarcity in the South Saskatchewan River Basin. *J. Water Resour. Plan. Manag.* **2011**, *137*, 92–100. [CrossRef]

14. Wheater, H.; Gober, P. Water security in the Canadian Prairies: Science and management challenges. *Philos. Trans. R. Soc. A Math. Phys. Eng. Sci.* **2013**, *371*, 20120409. [CrossRef]

15. Ottenbreit, G. *Water Security Agency: Plan for 2020–2021*; Water Security Agency: Moose Jaw, SK, Canada, 2020.

16. Lemmen, D.S.; Vance, R.E.; Campbell, I.A.; David, P.P.; Pennock, D.J.; Sauchyn, D.J.; Wolfe, S.A. *Geomorphic Systems of the Palliser Triangle, Southern Canadian Prairies: Description and Response to Changing Climate*; Natural Resources Canada/ESS/Scientific and Technical Publishing Services: Ottawa, ON, Canada, 1998.

17. Pomeroy, J.W.; Shook, K.R. *Review of Lake Diefenbaker Operations 2010–2011*; Centre for Hydrology, University of Saskatchewan: Saskatoon, SK, Canada, 2012.

18. Martin, F. *Gross Evaporation for the 30-Year Period 1971–2000 in the Canadian Prairies*; Hydrology Report #143; Prairie Farm Rehabilitation Administration: Regina, SK, Canada, 2002.

19. Saskatchewan Watershed Authority (SWA). *Lake Diefenbaker Reservoir Operations: Context and Objectives*; Hydrology and Groundwater Services: Swift Current, SK, Canada, 2012.

20. Western Economic Diversification Canada (WD). *Prairie Prosperity: A Vision for the Management of Water Resources across Saskatchewan and the Prairies*; Western Economic Diversification Canada: Edmonton, AB, Canada, 2020.

21. Ito, M.; Azam, S. Feasibility of Saline Gradient Solar Ponds as Thermal Energy Sources in Saskatchewan, Canada. *J. Environ. Inform. Lett.* **2019**, *1*, 72–80. [CrossRef]

22. Schmugge, T.; Andre, J.C. *Land Surface Evaporation*; Springer: New York, NY, USA, 1991.

23. Seo, Y. Effect of hydraulic diameter of flow straighteners on turbulence intensity in square wind tunnel. *HVAC Res.* **2013**, *19*, 141–147.

24. Komatsu, T.S. Toward a Robust Phenomenological Expression of Evaporation Efficiency for Unsaturated Soil Surfaces. *J. Appl. Meteorol.* **2003**, *42*, 1330–1334. [CrossRef]

25. An, N.; Hemmati, S.; Cui, Y.-J. Assessment of the methods for determining net radiation at different time-scales of meteorological variables. *J. Rock Mech. Geotech. Eng.* **2017**, *9*, 239–246. [CrossRef]

26. Mort, K.W.; Eckert, W.T.; Kelly, M.W. The steady-state flow quality of an open return wind tunnel model. *Can. Aeronaut. Space J.* **1972**, *18*, 285–289.

27. Schneider, K.; Ippisch, O.; Roth, K. Novel evaporation experiment to determine soil hydraulic properties. *Hydrol. Earth Syst. Sci.* **2006**, *10*, 817–827. [CrossRef]

28. Wickern, G.; Von Heesen, W.; Wallmann, S. Wind Tunnel Pulsations and their Active Suppression. *SAE Tech. Pap. Ser.* **2000**, *109*, 1403–1416. [CrossRef]

29. Teng, J.; Yasufuku, N.; Zhang, S.; He, Y. Modelling water content redistribution during evaporation from sandy soil in the presence of water table. *Comput. Geotech.* **2016**, *75*, 210–224. [CrossRef]

30. Lozada, C.; Caicedo, B.; Thorel, L. A new climatic chamber for studying soil–atmosphere interaction in physical models. *Int. J. Phys. Model. Geotech.* **2019**, *19*, 286–304. [CrossRef]

31. Salam, R.A.; Munir, M.M.; Warsahemas, T.; Saputra, C.; Latief, H.; Khairurrijal, K. A simple solar simulator with highly stable controlled irradiance for solar panel characterization. *Meas. Control.* **2019**, *52*, 159–168. [CrossRef]

32. Rezek, G. Suction vs. Pressure Forced Air Cooling-Part II. *IEEE Trans. Parts Mater. Packag.* **2004**, *2*, 35–43. [CrossRef]

33. İnan, M.; Atayilmaz, Ö.S. Experimental investigation of evaporation from a horizontal free water surface. *Sigma J. Eng. Nat. Sci.* **2017**, *35*, 119–131.

34. Lu, G.Y.; Wong, D.W. An adaptive inverse-distance weighting spatial interpolation technique. *Comput. Geosci.* **2008**, *34*, 1044–1055. [CrossRef]

35. Manwell, J.F.; McGowan, J.G.; Rogers, A.L. *Wind Energy Explained*; Wiley: New York, NY, USA, 2010.

36. Snyder, R.L. *Humidity Conversion*; UC Davis Biometeorology Group: Davis, CA, USA, 2005.

37. Hulley, G. *MYD21A2 MODIS/Aqua Land Surface Temperature/3-Band Emissivity 8-Day L3 Global 1 km SIN Grid V006*; NASA EOSDIS Land Processes DAAC: Oak Ridge, TN, USA, 2017.

38. Mohamed, A.A.; Sasaki, T.; Watanabe, K. Solute Transport through Unsaturated Soil due to Evaporation. *J. Environ. Eng.* **2000**, *126*, 842–848. [CrossRef]

39. Stannard, D.I.; Rosenberry, D.O.; Winter, T.C.; Parkhurst, R.S. Estimates of fetch-induced errors in Bowen-ratio energy-budget measurements of evapotranspiration from a prairie wetland, Cottonwood Lake Area, North Dakota, USA. *Wetlands* **2004**, *24*, 498–513. [CrossRef]

40. Patel, S.S.; Rix, A.J. The Impact of Water Surface Albedo on Incident Solar Insolation of a Collector Surface. In Proceedings of the 2020 International SAUPEC/RobMech/PRASA Conference, Cape Town, South Africa, 29–31 January 2020; pp. 1–6.

41. Finch, J.W. A comparison between measured and modelled open water evaporation from a reservoir in south-east England. *Hydrol. Process.* **2001**, *15*, 2771–2778. [CrossRef]

42. Lawrence, M.G. The Relationship between Relative Humidity and the Dewpoint Temperature in Moist Air: A Simple Conversion and Applications. *Bull. Am. Meteorol. Soc.* **2005**, *86*, 225–234. [CrossRef]

43. Yuan, W.; Zheng, Y.; Piao, S.; Ciais, P.; Lombardozzi, D.; Wang, Y.; Ryu, Y.; Chen, G.; Dong, W.; Hu, Z.; et al. Increased atmospheric vapor pressure deficit reduces global vegetation growth. *Sci. Adv.* **2019**, *5*, eaax1396. [CrossRef]

44. Granger, R.; Gray, D. Evaporation from natural nonsaturated surfaces. *J. Hydrol.* **1989**, *111*, 21–29. [CrossRef]
45. Singh, V.P.; Xu, C. Evaluation and generalization of 13 mass-transfer equations for determining free water evapo-ration. *Hydrol. Process.* **1997**, *11*, 311–323. [CrossRef]
46. Penman, H.L. Natural evaporation from open water, bare soil and grass. In *Proceedings of the Royal Society of London. Series A, Containing Papers of a Mathematical and Physical Character*; The Royal Society: London, UK, 1948; Volume 193, pp. 120–145.
47. Monteith, J.L. Evaporation and environment. *Symp. Soc. Exp. Biol.* **1965**, *19*, 205–234.
48. Himus, G.W.; Hinchley, J.W. The effect of a current of air on the rate of evaporation of water below the boiling point. *J. Soc. Chem. Ind.* **2007**, *43*, 840–845. [CrossRef]
49. Meyer, A.F. *Evaporation from Lakes and Reservoirs*; Minnesota Resources Commission: St. Paul, MN, USA, 1942.
50. De Bruin, H.A.R.; Keijman, J.Q. The Priestley-Taylor Evaporation Model Applied to a Large, Shallow Lake in the Netherlands. *J. Appl. Meteorol.* **1979**, *18*, 898–903. [CrossRef]
51. Duan, Z.; Bastiaanssen, W.G.M. Evaluation of three energy balance-based evaporation models for estimating monthly evaporation for five lakes using derived heat storage changes from a hysteresis model. *Environ. Res. Lett.* **2017**, *12*, 024005. [CrossRef]
52. Parsons, G.F.; Kulshreshtha, S.; Pentland, R.; Toma, D.; Hill, D.; McDonald, D.; Vogelsang, G.; Kent, D.; Schneider, K.; Thorp, T. *The Economic, Social and Environmental Benefits of Expanding Irrigation in the Lake Diefenbaker Region*; Saskatchewan Irrigation Projects Association: Central Butte, SK, Canada, 2008.
53. Abtew, W.; Melesse, A. *Evaporation and Evapotranspiration*; Springer: New York, NY, USA, 2013.